The Astronomical Journal, 170:1 (15pp), 2025 July https://doi.org/10.3847/1538-3881/add2ef

Searching for GEMS: Two Super-Jupiters Around M Dwarfs that May have Formed via Gravitational Instability

Andrew Hotnisky[1,2], Shubham Kanodia[3], Jessica Libby-Roberts[1,2], Suvrath Mahadevan[1,2,4], Caleb I. Cañas[5,21], Arvind F. Gupta[6], Te Han[7], Henry A. Kobulnicky[8], Alexander Larsen[8], Paul Robertson[7], Michael Rodruck[9], Gudmundur Stefansson[10], William D. Cochran[11,12], Megan Delamer[1,2], Scott A. Diddams[13,14], Rachel B. Fernandes[1,2,22], Samuel Halverson[2,15], Leslie Hebb[16], Andrea S.J. Lin[1,2], Andrew Monson[17], Joe P. Ninan[18], Arpita Roy[19], and Christian Schwab[20]

[1] Department of Astronomy & Astrophysics, 525 Davey Laboratory, The Pennsylvania State University, University Park, PA 16802, USA
[2] Center for Exoplanets and Habitable Worlds, 525 Davey Laboratory, The Pennsylvania State University, University Park, PA 16802, USA
[3] Earth and Planets Laboratory, Carnegie Science, 5241 Broad Branch Road, NW, Washington, DC 20015, USA
[4] Astrobiology Research Center, 525 Davey Laboratory, The Pennsylvania State University, University Park, PA 16802, USA
[5] NASA Goddard Space Flight Center, 8800 Greenbelt Road, Greenbelt, MD 20771, USA
[6] U.S. National Science Foundation National Optical-Infrared Astronomy Research Laboratory, 950 North Cherry Avenue, Tucson, AZ 85719, USA
[7] Department of Physics & Astronomy, The University of California, Irvine, CA 92697, USA
[8] Department of Physics & Astronomy, University of Wyoming, Laramie, WY 82070, USA
[9] Department of Physics, Engineering, and Astrophysics, Randolph-Macon College, Ashland, VA 23005, USA
[10] Anton Pannekoek Institute for Astronomy, University of Amsterdam, Science Park 904, 1098 XH Amsterdam, The Netherlands
[11] McDonald Observatory and Department of Astronomy, The University of Texas at Austin, USA
[12] Center for Planetary Systems Habitability, The University of Texas at Austin, USA
[13] Electrical, Computer & Energy Engineering, University of Colorado, 425 UCB, Boulder, CO 80309, USA
[14] Department of Physics, University of Colorado, 2000 Colorado Avenue, Boulder, CO 80309, USA
[15] Jet Propulsion Laboratory, 4800 Oak Grove Drive, Pasadena, CA 91109, USA
[16] Department of Physics, Hobart and William Smith Colleges, 300 Pulteney Street, Geneva, NY 14456, USA
[17] Steward Observatory, The University of Arizona, 933 North Cherry Avenue, Tucson, AZ 85721, USA
[18] Department of Astronomy and Astrophysics, Tata Institute of Fundamental Research, Homi Bhabha Road, Colaba, Mumbai 400005, India
[19] Astrophysics & Space Institute, Schmidt Sciences, New York, NY 10011, USA
[20] School of Mathematical and Physical Sciences, Macquarie University, Balaclava Road, North Ryde, NSW 2109, Australia
Received 2024 October 22; revised 2025 February 20; accepted 2025 March 16; published 2025 June 2

Abstract

We present the discovery of TOI-6303b and TOI-6330b, two massive transiting super-Jupiters orbiting a M0 and a M2 dwarf star, respectively, as part of the Searching for Giant Exoplanets around M-dwarf Stars (GEMS) survey. These were detected by NASA's Transiting Exoplanet Survey Satellite and then confirmed via ground-based photometry and radial velocity observations with the Habitable-zone Planet Finder. TOI-6303b has a mass of 7.84 ± 0.31 M_J, a radius of 1.03 ± 0.06 R_J, and an orbital period of 9.485 days. TOI-6330b has a mass of 10.00 ± 0.31 M_J, a radius of 0.97 ± 0.03 R_J, and an orbital period of 6.850 days. We put these planets in the context of super-Jupiters around M dwarfs discovered from radial-velocity surveys, as well as recent discoveries from astrometry. These planets have masses that can be attributed to two dominant planet formation mechanisms —gravitational instability and core accretion. Their masses necessitate massive protoplanetary disks that should either be gravitationally unstable, i.e., forming through gravitational instability, or be among the most massive protoplanetary disks known to date to form objects through core accretion. We also discuss their possible migration mechanisms via their eccentricity distribution.

Unified Astronomy Thesaurus concepts: Exoplanet astronomy (486); Exoplanets (498); Hot Jupiters (753); Radial velocity (1332); Transits (1711); M dwarf stars (982)

1. Introduction

M dwarfs are the most abundant stars in the Milky Way (T. J. Henry et al. 2006; C. Reylé et al. 2021). Searches for habitable and Earth-like worlds largely focus on these systems due to the close-in nature of their habitable zones (HZs; J. F. Kasting et al. 1993; J. Scalo et al. 2007; R. K. Kopparapu et al. 2013; A. C. Childs et al. 2022), and relatively higher planetary detection amplitudes through deeper transit dips, larger RV semiamplitudes, and more advantageous star–planet contrast ratios when compared to FGK stars. Previous efforts have provided occurrence rates of terrestrial planets around these types of stars (C. D. Dressing & D. Charbonneau 2015; K. K. Hardegree-Ullman et al. 2019; D. C. Hsu et al. 2020; K. Ment & D. Charbonneau 2023), even though the occurrence rate of habitable-zone planets around M-dwarf stars is still debated (G. J. Bergsten et al. 2023).

HZ/terrestrial planets can be affected by their giant planet companions (A. C. Childs et al. 2019; M. Schlecker et al. 2021; B. Bitsch & A. Izidoro 2023). Around M dwarfs, giant and terrestrial planets have yet to be seen in the same system. This is derived from a lack of observed giant exoplanets around M-dwarf stars (GEMS). An increase in observed

[21] NASA Postdoctoral Fellow.
[22] President's Postdoctoral Fellow.

Table 1
Summary of Ground-based Photometry

Object Name	Obs Date (YYYY-MM-DD)	Filter	Exposure Time (s)	PSF FWHM (″)	Field of View (′)	Telescope
TOI-6330	2023-11-08	Bessel I	240	2.0 – 2.8	8.94 × 8.94	RBO (0.6 m)
TOI-6330	2023-11-08	Kron/Cousins I	172	3.8 – 4.9	15.9 × 10.75	Keeble (0.4 m)
TOI-6303	2023-12-29	Bessel I	240	1.8 – 2.7	8.94 × 8.94	RBO (0.6 m)
TOI-6330	2024-01-29	Semrock	40	5.1 – 9.1	7.9 × 7.9	APO (3.5 m)

GEMS with precise mass measurements and orbital characteristics would enhance our ability to determine the frequency of giant planets around M dwarfs and the effects terrestrial and giant planets have on one another. Additionally, we would increase our understanding of giant planet formation around M dwarfs.

Core accretion is the commonly accepted formation pathway for close-in giant planets ($\gtrsim$8 $R_\oplus$) (D. A. Fischer & J. Valenti 2005; M. Narang et al. 2018). This formation is a "bottom-up" approach to planetary formation where an $\sim$10 $M_\oplus$ core is accreted followed by an exponential gas accretion that forms the planet's gaseous envelope. The alternate mode of formation is the gravitational instability (GI) scenario (A. P. Boss 1997, 2006), which occurs in the protostellar phase of massive disks where the disk fragments into gravitationally bound clumps. It is expected that core accretion should produce fewer GEMS than gas giants around FGK-dwarfs because of lower disk masses and longer orbital timescales, causing it to be more difficult to reach the exponential runaway gas accretion (G. Laughlin et al. 2004; S. Ida & D. N. C. Lin 2005). NASA's Transiting Exoplanet Survey Satellite (TESS; G. R. Ricker et al. 2014) has enabled the discovery of many Jupiter-sized exoplanets (e.g., C. I. Cañas et al. 2020; M. J. Hobson et al. 2023; S. Kanodia et al. 2023; M. Delamer et al. 2024) and brown dwarfs (e.g., E. Artigau et al. 2021; C. I. Cañas et al. 2022) orbiting M-dwarf stars, which have already started to raise interesting questions about the formation and evolution of these planets (R. H. Durisen et al. 2007; G. Chabrier et al. 2014). However, the current sample size ($\sim$30) is insufficient to enable a comprehensive understanding of these systems. We have therefore started the volume limited (<200 pc) Searching for GEMS survey (S. Kanodia et al. 2024), to increase the sample size of these planets to $\sim$40 transiting GEMS. This will enable robust statistical comparisons of these planets with their FGK counterparts, thereby helping shed light on their formation mechanisms.

Studies of giant planet dependence on host-star metallicity have shown that the region between $\sim$4 and 10 M_J is sparsely populated by giant planets for FGK host stars (N. C. Santos et al. 2017; M. Narang et al. 2018; K. C. Schlaufman 2018). It is believed that this marks the transition between the two giant planet formation mechanisms—core accretion and GI. This is because the objects below 4 M_J are believed to have formed through core accretion, whereas those above 10 M_J are formed through GI (N. C. Santos et al. 2017; M. Narang et al. 2018; K. C. Schlaufman 2018).

As part of the Searching for GEMS survey, we present the discovery of two super-Jupiters around early M dwarfs—TOI-6303b at 7.84 ± 0.31 M_J and TOI-6330b at 10.00 ± 0.32 M_J. These objects populate the upper limit of the transition zone between core accretion and GI. In Section 2, we present our observations of both systems. We detail our photometric observations from TESS, RBO, the Astrophysical Research Consortium Telescope Imaging Camera (ARCTIC; J. Huehnerhoff et al. 2016) on the 3.5 m telescope at Apache Point Observatory (APO), Keeble observatory, precision radial velocities from the Habitable-zone Planet Finder (HPF), and high-contrast speckle imaging from Shane Adaptive Optics (ShaneAO) and NN-EXPLORE Exoplanet Stellar Speckle Imager (NESSI). In Section 3, we detail the analysis performed to obtain the stellar parameters and the planetary parameters. In Section 4, we discuss the possible formation paths of these objects and place them in context of the giant exoplanets and brown dwarfs. Finally, we summarize our discovery in Section 5.

2. Observations

2.1. Tess

TOI-6303 (TIC-186810676) and TOI-6330 (TIC-308120029) were observed in Sector 18 at 1800 s cadence from 2019 November 3 to 27 and in Sector 58 at 200 s cadence from 2022 October 29 to November 26. Both planet candidates were flagged using the Quick Look Pipeline (C. X. Huang et al. 2020) through the Faint-Star Search (M. Kunimoto et al. 2022).

We obtain the light curves using `eleanor` (A. D. Feinstein et al. 2019) by extracting a 31×31 pixels cut-out from calibrated TESS full-frame images. Meanwhile, `eleanor` adopted aperture settings of a 2×1 pixel rectangle for TOI-6330 and a 3×3 pixel square for TOI-6303 because these apertures minimized the combined differential photometric precision on 1 hr long timescales and the background-subtracted photometry corrected for systematics (CORR_FLUX) to derive the light curves from both sectors for both objects (Figure 1).

TOI-6303 and TOI-6330 both lie in a sparse region of the sky with the nearest star being $\sim$17″ and $\sim$10″ away, respectively (Gaia Collaboration et al. 2021). These close by stars are still blended in the 21″×21″ TESS pixel, which can be seen in the TESS light curves (see Figure 2). This dilution is corrected using ground-based photometry, as discussed in Section 2.2.

2.2. Ground-based Photometry

We observe one transit of TOI-6303 and three transits of TOI-6330 from the ground to confirm TOI-6303 and TOI-6330 as the host stars for the TESS-identified transit events, as well as correct for undiluted transit depths (see Section 3.2). Table 1 provides an overview of both targets' observations, telescope, and instrumental setup.

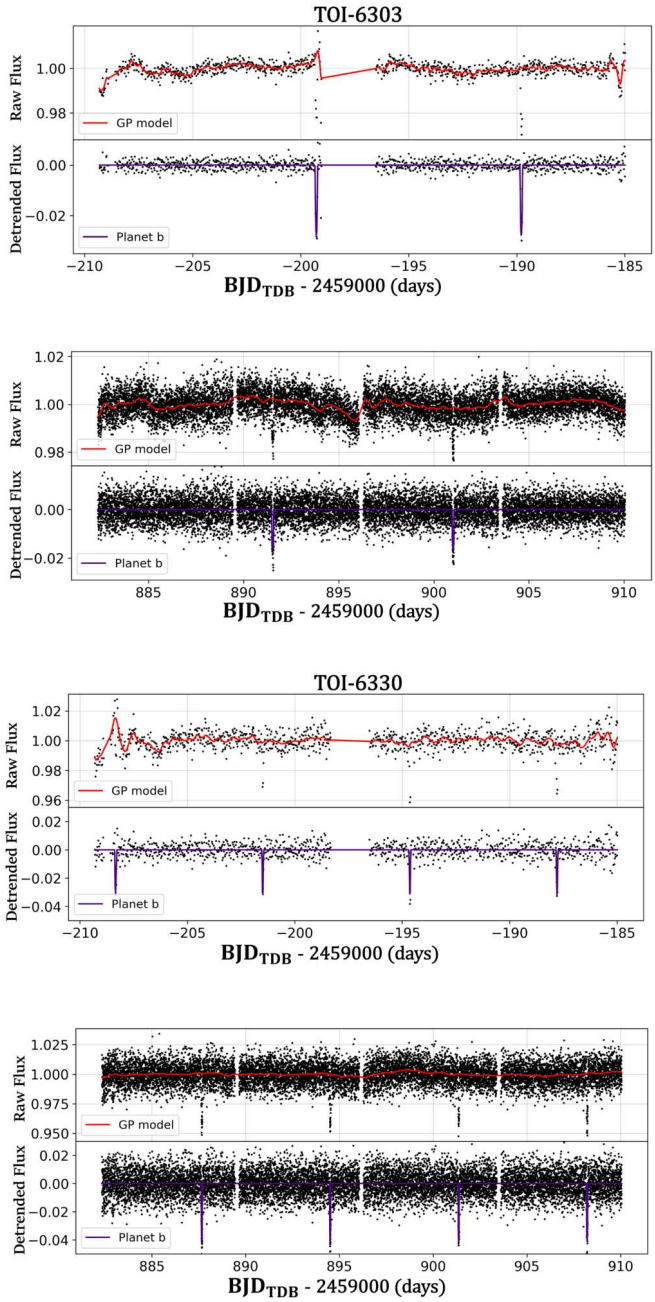

Figure 1. The TOI-6303 and TOI-6330 light curves processed using `eleanor` for TESS Sectors 18 (the top subfigure with an 1800 s exposure time) and 58 (the bottom subfigure with a 200 s exposure time). The top panel of each sector's light curve is a rotation Gaussian process kernel that is used to remove both astrophysical and instrumental systematics in the light curve labeled `RotationTerm` from `celerite2` (seen in red). The bottom panel is the best-fit Gaussian process-subtracted photometry for the transit of TOI-6303b and TOI-6330b.

2.2.1. Red Buttes Observatory

We observed one transit of TOI-6303b and one transit of TOI-6330b using the Red Buttes Observatory (RBO) 0.6 m telescope in Wyoming (D. H. Kasper et al. 2016). The TOI-6303b transit was observed on the night of 2023 December 29 and the TOI-6330b transits were observed on the night of 2023 November 8 with observation details in Table 1.

The observations were processed by first bias and dark subtracting each image, and then dividing by a median-combined normalized dome-flat. Then, we looped-over randomly selected reference stars and aperture sizes to minimize the rms scatter in the processed light curve. Further details on this processing method are described by A. J. Monson et al. (2017). The TOI-6330b light curve was further detrended by masking out the transit and dividing out an instrumental linear trend in the baseline. The final light curves are plotted in Figure 2.

2.2.2. Apache Point Observatory

We observed a transit of TOI-6330b on the night of 2024 January 29 using APO/ARCTIC. We utilized the Semrock filter (842 to 873 nm; G. Stefansson et al. 2017) with an exposure time of 40 s and airmass increased from 1.6 to 5.7. The Semrock filter bandpass minimizes overlap with

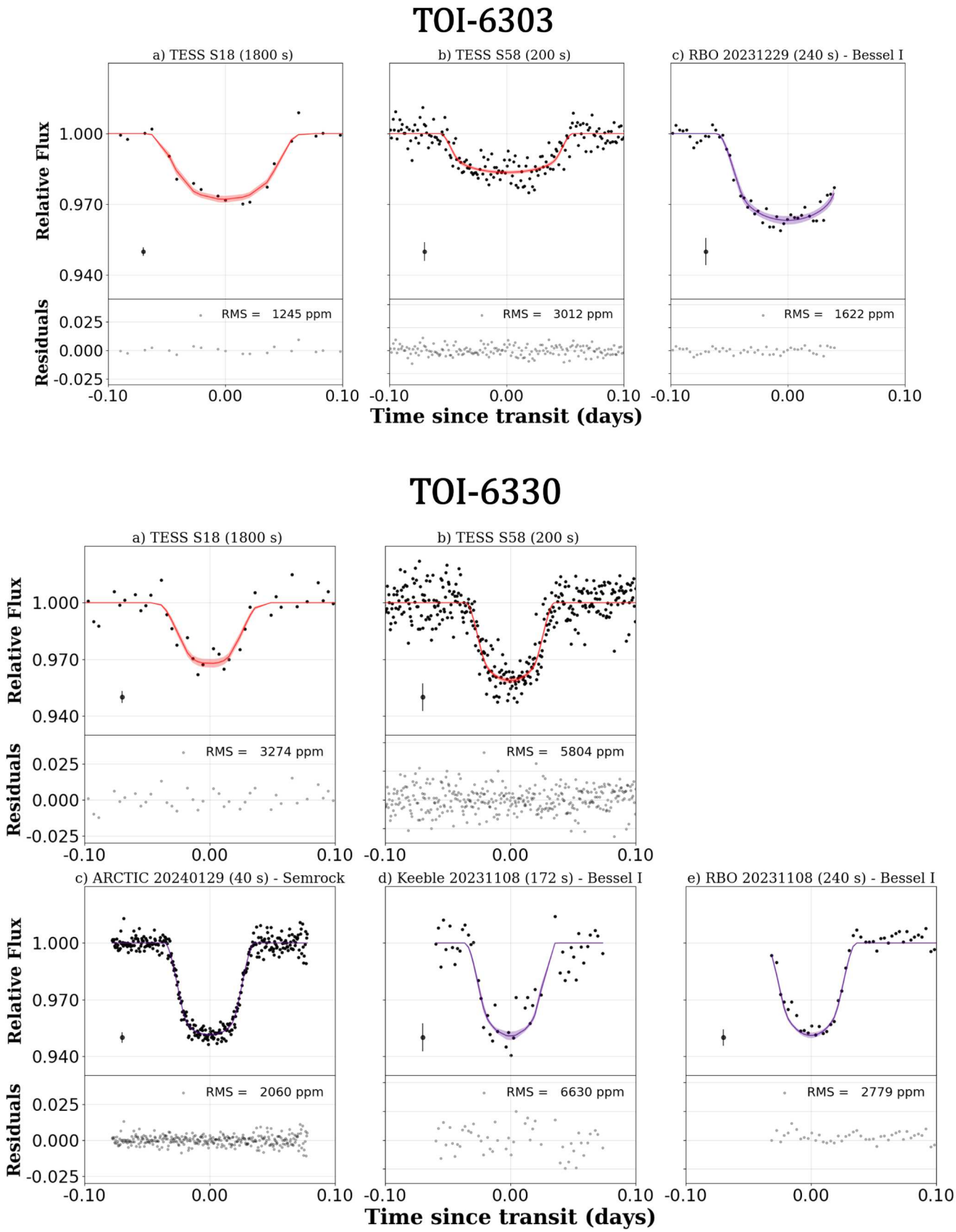

Figure 2. The TOI-6303b and TOI-6330b phase-folded photometric observations. The TESS phase-folded light curves are shown in subfigures (a) and (b) for Sectors 18 and 58, respectively. The black points show the detrended data and the purple line details the model with a 1σ uncertainty in the translucent-purple region. We show the median uncertainty at -0.07 days. The red models for the TESS light curves indicate a floating dilution term, which is constrained with the data sets in purple.

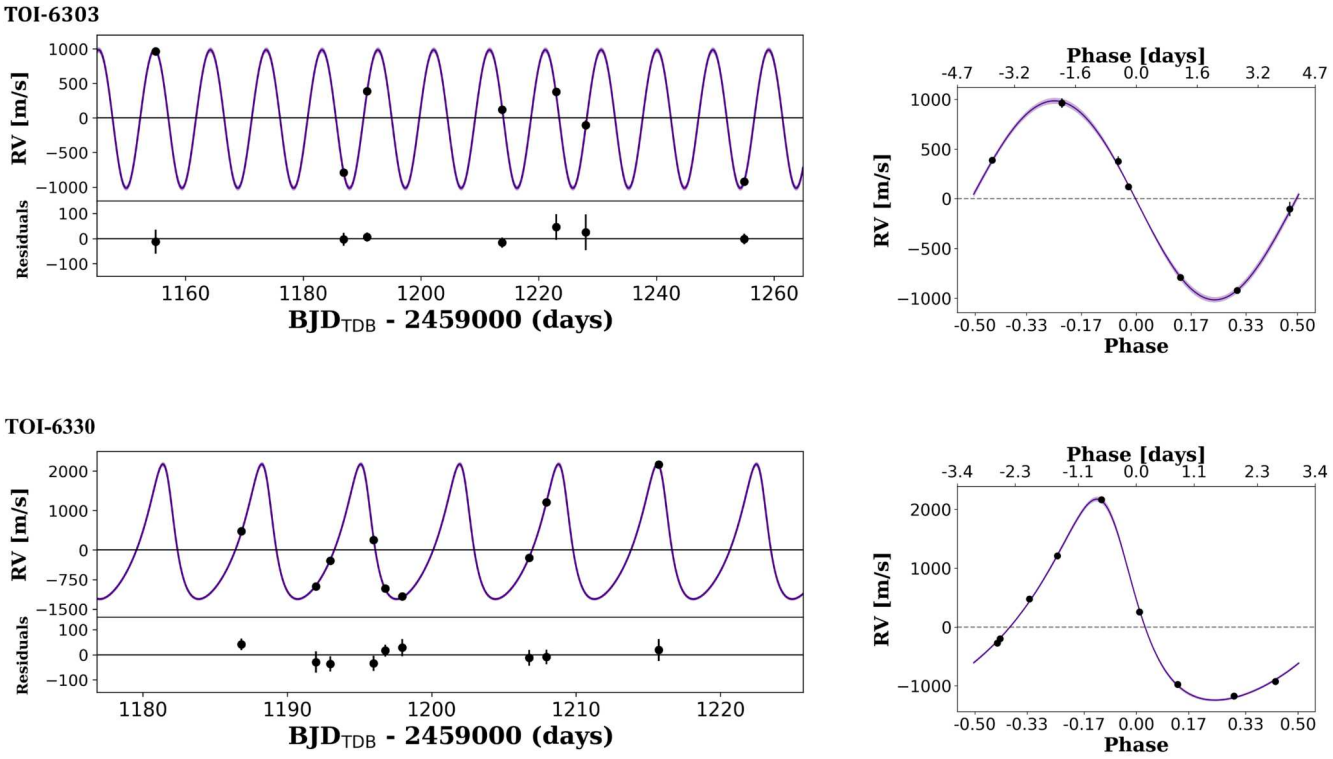

Figure 3. Left: An RV time series for TOI-6303 (top) and TOI-6330 (bottom) as observed by HPF. The model best fit is designated by the purple line with a lighter purple indicating the 16%–84% uncertainty. The error bars along the time series model are difficult to see because they are small compared to the *y*-axis spread. For TOI-6303, the observations with larger error bars are one 15 minutes exposure while the rest are two binned 15 minutes exposures (see Table 2). Right: Phase-folded HPF RVs on best-fit orbital parameters (top: TOI-6303, bottom: TOI-6330). We set the eccentricity and argument of periastron to float. TOI-6303 is consistent with a circular orbit, while TOI-6330 shows an eccentric orbit.

atmospheric water-band features, reducing photometric scatter due to varying airmass or atmospheric water columns. The exposures were captured utilizing 4×4 binning. We used the fast readout mode, which allowed us to obtain a readout time of 1.3 s, a gain of 2 e^-/ADU, and a plate scale of $0\farcs456$ pixel^{-1}.

We bias subtracted and flat fielded the data using `AstroImageJ` (K. A. Collins et al. 2017). We performed differential photometry with an aperture radius of 8 pixels ($3\farcs65$) and an inner sky radius of 14 pixels ($6\farcs38$) alongside an outer sky radius of 20 pixels ($9\farcs12$) used to subtract the star's background. We calculated the flux uncertainties using a combination of photon noise, detector read noise, and airmass (G. Stefansson et al. 2017). The light curve is plotted on the bottom right of Figure 2.

2.2.3. Keeble Observatory

We observed a transit of TOI-6330b on 2023 November 8 using the 0.4 m telescope at the Randolph-Macon College's Keeble Observatory in Ashland, Virginia. We used the Kron/Cousins *I*-Band filter with an exposure time of 172 s. The observations were obtained using 2×2 binning with an airmass decreasing from 1.3 to 1.0. We made our observations with a plate scale of $0\farcs88$ and a gain of $1.3e^-$/ADU. The data were reduced and analyzed using `AstroImageJ` (K. A. Collins et al. 2017) following the same procedure as APO (Section 2.2.2). We used an aperture radius of 8 pixels ($7\farcs032$), an inner sky radius of 15 pixels ($13\farcs185$), and an outer sky radius of 20 pixels ($17\farcs58$). See the bottom middle panel in Figure 2 for the light curve.

2.3. Radial Velocity

2.3.1. HPF

We obtained radial velocity (RV) observations for TOI-6303 and TOI-6330 using the HPF (S. Mahadevan et al. 2012, 2014) located at the 10 m Hobby–Eberly Telescope (HET; L. W. Ramsey et al. 1998). HPF is a near-infrared (NIR), environmentally stabilized (G. Stefansson et al. 2016), fiber-fed (S. Kanodia et al. 2018), high-resolution precision spectrograph with a resolution of 55,000 spanning from 810 to 1280 nm. HPF is fully queue-scheduled with HET resident astronomers executing all observations (M. Shetrone et al. 2007).

TOI-6303 was observed seven times between 2023 July 29 and November 6 with an exposure time of 945 s. Four of the seven observations consist of two subsequent exposures, which were later binned postprocessing to minimize noise. The remaining three observations are low signal-to-noise ratio single-exposures due to poor weather and sky conditions. TOI-6330 was observed nine times between 2023 August 30 and September 28, with each visit consisting of two exposures of 945 s each. The RVs from individual exposures were combined by weighted averaging for each night.

The data were processed using the `HxRGproc` package (J. P. Ninan et al. 2018). The barycentric corrections were performed with `barycorrpy` (S. Kanodia & J. Wright 2018), which is the Python implementation of the algorithms

Table 2
The 30 minutes Weighted-average Binned HPF RVs of TOI-6303 and TOI-6330

Date (BJD_{TDB})	RV ($m\ s^{-1}$)	σ_{RV} ($m\ s^{-1}$)
TOI-6303		
2460154.94681[a]	−967	48
2460186.86262	−785	25
2460190.85569	393	18
2460213.80174	126	20
2460222.98768[a]	382	51
2460227.98737[a]	−100	71
2460254.91193	−915	21
TOI-6330		
2460186.81214	271	24
2460191.98574	−1132	42
2460192.98611	−481	30
2460195.97687	48	30
2460196.78045	−1185	24
2460197.96543	−1381	34
2460206.74331	−408	31
2460207.94776	1004	29
2460215.72917	1958	44

Note. Observations denoted with an [a] have a single 15 minutes exposure.

from J. T. Wright & J. D. Eastman (2014). We did not use the NIR Laser Frequency Comb (A. J. Metcalf et al. 2019) for HPF due to concerns about scattered light.

We applied a version of the template-matching algorithm `SERVAL` (M. Zechmeister et al. 2018; G. Stefánsson et al. 2023), modified for HPF (A. J. Metcalf et al. 2019) to estimate the RVs from the spectra for both systems. Using this method, we first create a master template of all observations and then compare the Doppler shift of each spectra to the master template to minimize χ^2 statistics. The master template is constructed after the masking of the telluric and sky-emission lines. Our final binned RVs for TOI-6303 and TOI-6330 are listed in Table 2 and shown in Figure 3.

2.4. Speckle Imaging

To rule out nearby background sources or faint stellar companions, we obtained data from NESSI (N. J. Scott et al. 2018) located on the WIYN[23] 3.5 m telescope at Kitt Peak National Observatory and the ShARCS camera (S. Srinath et al. 2014) located on the Shane 3 m telescope at the University of California's Lick Observatory.

TOI-6303 observations occurred on 2024 February 17 and 2023 November 25 with NESSI and ShaneAO, respectively. The NESSI observations were a 9 minutes sequence of 40 ms exposures for both systems using Sloan *r*' and *z*' filters. We processed and combined the exposures using the method described by S. B. Howell et al. (2011). The ShaneAO observations were taken in laser guide star mode with a four-position dithering pattern for a total of 25 minutes exposure time in *Ks* filter. We detected no background sources with a separation $>1\farcs0$ and $\Delta Ks < 4.5$ for ShaneAO, and no background sources with a separation $>0\farcs3$ and $\Delta z', \Delta r' < 4.0$ for NESSI.

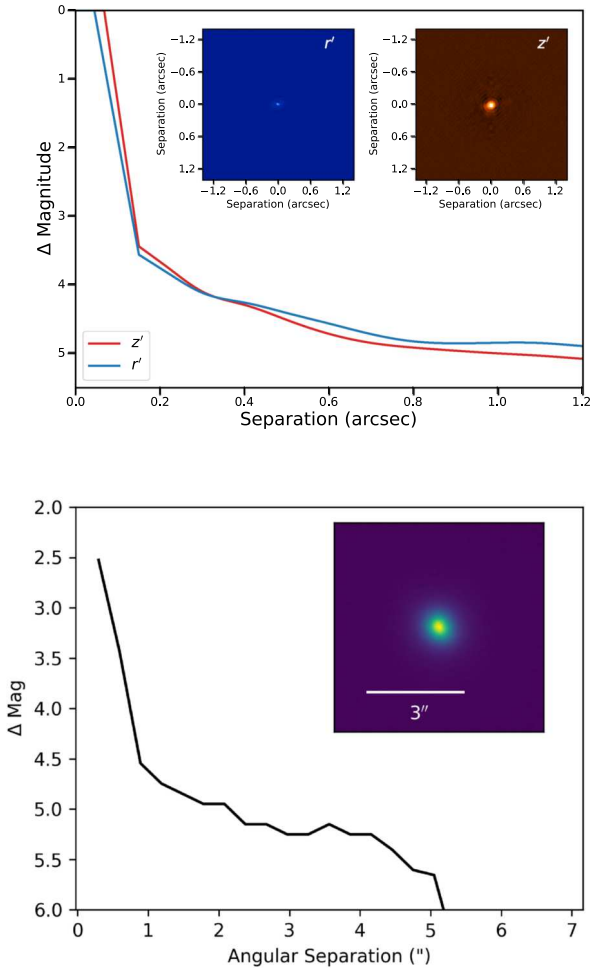

Figure 4. Top: 5σ processed contrast curve for TOI-6303 observed from NESSI in the Sloan *z*' and *r*' filters. Bottom: 5σ processed contrast curve for TOI-6303 observed from ShaneAO in the *Ks*-band.

TOI-6330 was observed on 2023 September 8 with NESSI with the same observation and postprocessing techniques as for the TOI-6303 observations. TOI-6330 was also observed on 2024 July 25 by ShaneAO in nonlaser guide star mode with five-position dithering for a total of 32 minutes exposure time in *Ks* filter. As for TOI-6303, we detected no background sources with a separation $>1\farcs0$ and $\Delta Ks < 5.25$ for ShaneAO and no background sources with a separation $0\farcs3$ and $\Delta z', \Delta r' < 4.0$. TOI-6303 and TOI-6330 contrast curves are seen in Figures 4 and 5.

3. Analysis

3.1. Stellar Parameters

The stellar parameters for both systems were determined using the `HPF-SpecMatch` package (G. Stefansson et al. 2020) for spectroscopic parameters. The fits were performed by matching the target spectra against a catalog of HPF spectra for GKM dwarfs to calculate a χ^2 value. This χ^2 value is then used to determine the five best catalog stars utilized to characterize TOI-6303 and TOI-6330. We estimate values for

[23] The WIYN Observatory is a joint facility of the NSF's National Optical-Infrared Astronomy Research Laboratory, Indiana University, the University of Wisconsin–Madison, Pennsylvania State University, Purdue University, and Princeton University.

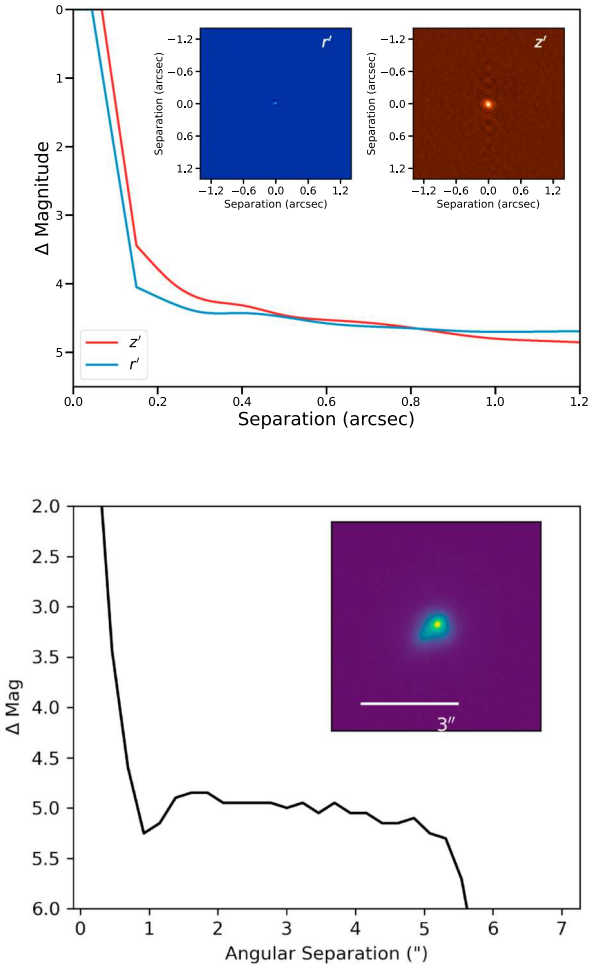

Figure 5. Top: 5σ processed contrast curve for TOI-6330 observed from NESSI in the Sloan z' and r' filters. Bottom: 5σ processed contrast curve for TOI-6330 observed from ShaneAO in the *Ks*-band.

the effective temperatures $T_{\rm eff}$, surface gravity $\log g$, metallicities [Fe/H], and projected rotational velocities v sin i_* for both systems (see Table 3). Due to the minimal telluric line contamination, we use HPF's Order 5 (8534–8645 Å) to fit our systems. HPF's instrumental resolution limits our v sin i_* to <2 km s^{-1}. Determining the metallicity for M dwarfs is exceptionally difficult (V. M. Passegger et al. 2022) yielding a recommendation to interpret the metallicities of these stars with caution. We therefore suggest a categorical classification for TOI-6303 and TOI-6330 as supersolar and solar metallicities, respectively.

We use the `ExoFASTv2` package (J. D. Eastman et al. 2019) to perform an SED and isochrones fit for the stellar physical parameters. The Gaussian priors for the SED fit we used were the spectroscopic parameters derived from `HPF-SpecMatch`, the distance calculated from C. A. L. Bailer-Jones et al. (2021) using the GAIA DR3 parallax, and the magnitudes listed in Table 3 (R. M. Cutri et al. 2003; E. L. Wright et al. 2010; E. A. Magnier et al. 2020). The stellar mass and radius for TOI-6303 and TOI-6330 are $0.644 \pm 0.024\ M_\odot$, $0.609 \pm 0.016\ R_\odot$ and $0.531 \pm 0.021\ M_\odot$, and $0.490 \pm 0.011\ R_\odot$, respectively. Physical parameters for both stars are detailed in Table 3.

We utilized ground-based monitoring with the Zwicky Transient Facility (ZTF; F. J. Masci et al. 2019) alongside

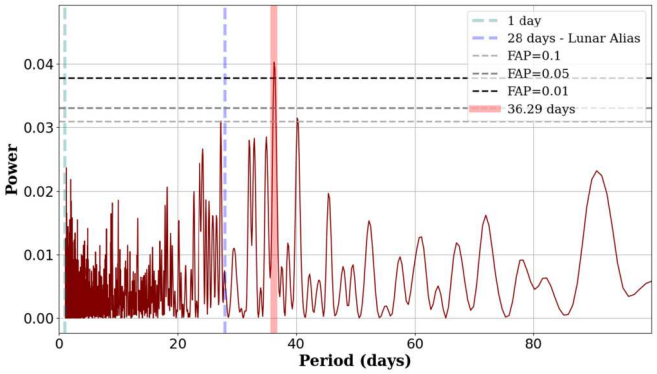

Figure 6. The TOI-6330 ZTF periodogram with the ZTF-r filter. The teal and blue vertical lines detail the 1 and 28 days periods, respectively. The red highlight shows a peak period at 36.29 days believed to be from stellar activity. The horizontal dashed lines detail the 10%, 5%, and 1% FAPs from bottom to top. The ZTF data is obtained directly from the ZTF database via IRSA.

TESS to search for rotational variability in the photometry. We do not detect a significant peak in the ZTF periodogram for TOI-6303 in either the ZTF-r or ZTF-g filters. From the HPF limit of v sin $i_* < 2$ km s^{-1}, TOI-6303 has a lower limit rotation period of $\sim$15 days assuming a near 90° inclination; however, given the nondetection, the rotation period is likely longer than this minimum. We detect a peak above the 1% false alarm probability (FAP) line in the ZTF-r periodogram at an approximately 36 day rotation period for TOI-6330 (Figure 6). We also utilized the ZTF-g periodogram to attempt to detect any activity but there is no peak greater than the 10% FAP line. We believe this nondetection in the g-band is due to the faintness of the star alongside the possible interference of the lunar cycle. Furthermore, we do not detect any periodicity in the activity indicators measured by HPF-`SERVAL`. It is important to note with only nine binned observations, it is challenging to detect a 36 days rotation period with any confidence. The HPF limit of v sin $i_* < 2$ km s^{-1} yields a lower limit rotation period of $\sim$12 days assuming a near 90° inclination. We, therefore, cautiously suggest a 36 days rotation period for TOI-6330.

We use the renormalized unit weight error (RUWE) from Gaia DR3 (Gaia Collaboration et al. 2021) to determine the likelihood of a blended companion leading to excess astrometric noise. An RUWE value of $\sim$1 is consistent with a single star while a value $>$1.4 is a conservative threshold indicating a massive companion (V. Belokurov et al. 2020; C. Ziegler et al. 2020). TOI-6303 and TOI-6330 have RUWE values of 1.01 and 1.05, respectively, indicating a single source with no additional light blending into the transits from other stars for both systems.

The regions in which TOI-6303 and TOI-6330 are located are sparse regions of the sky and none of the resolved companions in Gaia DR3 within 60″ have similar proper motions or parallaxes.

3.2. Joint Fit of RVs and Photometry: Planetary Parameters

We performed a joint fit of all transit data from TESS and ground-based photometry alongside HPF RVs using the `exoplanet` package (D. Foreman-Mackey et al. 2021a) for both systems. We detrended the TESS photometry using a Gaussian process `RotationTerm` kernel before the joint fit while masking out the transiting events (D. Foreman-Mackey

Table 3
Summary of Stellar Parameters

Parameter	Description	TOI-6303	TOI-6330	Reference
Main Identifiers:				
TIC	TESS Input Catalogue	TIC-186810676	TIC-308120029	Stassun
2MASS	⋯	2MASS J03070731+4008503	2MASS J01284037+5341105	2MASS
Gaia DR3	⋯	Gaia DR3 239050153051494272	Gaia DR3 407530931116600320	Gaia DR3
Equatorial Coordinates, Proper Motion, and Distance:				
α_{J2000}	R.A.	03:07:07.36	01:28:40.32	Gaia DR3
δ_{J2000}	decl.	+40:08:49.83	+53:41:09.88	Gaia DR3
μ_α	Proper motion (R.A., mas yr^{-1})	32.941 ± 0.069	-35.668 ± 0.164	Gaia DR3
μ_δ	Proper motion (decl., mas yr^{-1})	-35.375 ± 0.054	-45.0748 ± 0.073	Gaia DR3
ω	Parallax (mas)	6.587 ± 0.019	6.967 ± 0.027	Gaia DR3
d	Distance in pc	151.82 ± 0.42	143.51 ± 0.55	Bailer-Jones
$A_{V,\max}$	Maximum visual extinction	0.1	0.1	Green
Optical and NIR Magnitudes:				
V	Johnson V mag	14.6 ± 0.2	16.3 ± 0.2	APASS
G	Mean G mag	13.8979 ± 0.0004	14.9120 ± 0.0005	Gaia DR3
g'	Pan-STARRS1 g' mag	15.885 ± 0.0004	16.492 ± 0.0071	Pan-STARRS1
r'	Pan-STARRS1 r' mag	14.194 ± 0.002	15.317 ± 0.0026	Pan-STARRS1
i'	Pan-STARRS1 i' mag	13.607 ± 0.003	14.260 ± 0.0032	Pan-STARRS1
z'	Pan-STARRS1 z' mag	13.378 ± 0.005	13.772 ± 0.0016	Pan-STARRS1
J	J mag	11.679 ± 0.018	12.368 ± 0.023	2MASS
H	H mag	11.036 ± 0.017	11.744 ± 0.015	2MASS
K_s	K_s mag	10.826 ± 0.016	11.513 ± 0.023	2MASS
$W1$	WISE1 mag	10.747 ± 0.023	11.356 ± 0.021	WISE
$W2$	WISE2 mag	10.786 ± 0.026	11.299 ± 0.020	WISE
$W3$	WISE3 mag	10.25 ± 0.067	11.192 ± 0.136	WISE
`SpecMatch` Spectroscopic Parameters:				
$T_{\rm eff}$	Effective temperature in K	3977 ± 59	3539 ± 59	This work
[Fe/H]	Metallicity in dex	0.44 ± 0.16	0.08 ± 0.16	This work
$\log(g)$	Surface gravity in cgs units	4.67 ± 0.04	4.77 ± 0.04	This work
$v \sin i_*$	Rotational velocity in km s^{-1}	<2	<2	This work
$P_{\rm rot}$	Rotation Period in days	⋯	∼36	This work
Model-dependent Stellar SED and Isochrone Fit Parameters:				
M_*	Mass in $M_\odot$	0.644 ± 0.024	0.531 ± 0.021	This work
R_*	Radius in $R_\odot$	0.609 ± 0.016	0.490 ± 0.011	This work
L_*	Luminosity in $L_\odot$	0.0819 ± 0.0018	0.03701 ± 0.0009	This work
ρ_*	Density in g cm^{-3}	4.01 ± 0.28	6.02 ± 0.46	This work
Age	Age in Gyr	$6.4^{+4.7}_{-4.4}$	$7.6^{+4.2}_{-4.9}$	This work

Note. References are: Stassun (K. G. Stassun et al. 2018), 2MASS (R. M. Cutri et al. 2003), Gaia DR3 (Gaia Collaboration et al. 2021), Bailer-Jones (C. A. L. Bailer-Jones et al. 2021), Green (G. M. Green et al. 2019), APASS (A. A. Henden et al. 2018), Pan-STARRS1 (K. C. Chambers et al. 2016; E. A. Magnier et al. 2020), and WISE (E. L. Wright et al. 2010).

et al. 2017; D. Foreman-Mackey 2018). We fit each instrument with a quadratic limb darkening prior and a white noise jitter term (TESS Sectors + ground-based). The TESS sector pixels are large enough (>21″) to potentially cause contamination from neighboring stars, which we account for by including a dilution term for each TESS sector, which is estimated using the ground-based photometric data. Equation (1) in S. Kanodia et al. (2023) is used to account for dilution. We leave eccentricity and argument of periastron free for both systems and include additional terms for RV jitter, RV offset, and a linear RV trend.

To obtain the joint-fit parameters, we employ the `exoplanet` package (D. Foreman-Mackey et al. 2021a) using `pymc3` (J. Salvatier et al. 2016) and `theano` (The Theano Development Team et al. 2016) to perform MCMC sampling for both systems. We include the stellar mass (0.644 ± 0.024 $M_\odot$, 0.531 ± 0.021 $M_\odot$), stellar radius (0.609 ± 0.016 $R_\odot$, 0.490 ± 0.011 $R_\odot$), stellar temperature (3977 ± 59 K, 3539 ± 59 K), transit midpoint, orbital period, and transit depth (35 mmag, 36 mmag) as priors corresponding to TOI-6303b and TOI-6330b, respectively, for the posterior fits. We used four chains with 1500 burn in steps followed with an additional 4500 steps to confidently fit for the planetary parameters detailed in Table 4. To ensure our posteriors are well-mixed and independent, we analyze each parameter for convergence using the Gelman–Rubin statistic, where an $\hat{R} \sim 1$ represents a strong convergence (E. B. Ford 2006). We further check our stellar mass and radii using photometric relationships (Equation (5) from A. W. Mann et al. (2015) and A. W. Mann et al. 2019). We find a 1σ agreement for the radii and a 2σ agreement for the mass, giving us confidence in these reported values and uncertainties.

4. Discussion

TOI-6303b and TOI-6330b are the most massive transiting GEMS discovered, with masses of 7.84 ± 0.31 M_J and 10.00 ± 0.32 M_J, and mass ratios of 1.16% and 1.79%, respectively (Figure 7). In Figure 8, we plot these planets

Table 4
Derived Planetary Parameters

Parameter	Units	TOI-6303b	TOI-6330b
Instrument-Dependent Parameters:			
RV Trend	dv/dt (m s^{-1} yr^{-1})	$0.09^{+4.85}_{-4.94}$	$0.01^{+4.83}_{-4.86}$
HPF RV Offset	$\gamma_{\rm HPF}$ (m s^{-1})	$5.40^{+17.2}_{-15.7}$	$-207.27^{+15.73}_{-16.64}$
RV Jitter	$\sigma_{\rm HPF}$ (m s^{-1})	$24.3^{+34.7}_{-17.4}$	$30.2^{+27.7}_{-18.8}$
Transit Depth Dilution	$D_{\rm TESSS18}$	$0.76^{+0.39}_{-0.36}$	0.75 ± 0.06
	$D_{\rm TESSS58}$	0.45 ± 0.03	0.83 ± 0.03
Transit Jitter	$\sigma_{\rm TESS-S18}$	0.0061 ± 0.0003	0.0055 ± 0.0001
	$\sigma_{\rm TESS-S58}$	0.00458 ± 0.00003	0.00863 ± 0.00006
	$\sigma_{\rm APO}$	...	0.00205 ± 0.00022
	$\sigma_{\rm RBO}$	$0.00003^{+0.00025}_{-0.00003}$	$0.00003^{+0.00032}_{-0.00003}$
	$\sigma_{\rm Keeble}$	...	$0.00458^{+0.00220}_{-0.00446}$
Quadratic Limb Darkening	$[u, v]_{\rm TESS-S18}$	$[0.58^{+0.54}_{-0.40}, -0.002^{+0.43}_{-0.40}]$	$[0.22^{+0.28}_{-0.16}, 0.04^{+0.25}_{-0.18}]$
	$[u, v]_{\rm TESS-S58}$	$[0.58 \pm 0.36, 0.13 \pm 0.40]$	$[0.75^{+0.30}_{-0.36}, -0.04^{+0.46}_{-0.36}]$
	$[u, v]_{\rm APO}$	...	$[0.16^{+0.19}_{-0.12}, 0.70^{+0.16}_{-0.23}]$
	$[u, v]_{\rm RBO}$	$[0.66 \pm 0.39, 0.05^{+0.44}_{-0.39}]$	$[0.98^{+0.25}_{-0.33}, -0.30^{+0.41}_{-0.24}]$
	$[u, v]_{\rm Keeble}$	...	$[0.60^{+0.40}_{-0.38}, -0.03^{+0.41}_{-0.34}]$
Orbital Parameters:			
Orbital Period	P (days)	9.4852360 ± 0.0000162	6.8500246 ± 0.0000033
Eccentricity	e	0.02 ± 0.02	0.34 ± 0.01
Argument of Periastron	ω (radians)	$2.05^{+0.67}_{-4.50}$	$0.65^{+0.04}_{-0.03}$
Semiamplitude Velocity	K (m s^{-1})	1000 ± 27	1710 ± 30
Transit Parameters:			
Transit Midpoint	T_C (BJD$_{\rm TDB}$)	$2459901.01440 \pm 0.00011$	$2459901.36114 \pm 0.00021$
Scaled Radius	R_p/R_s	0.175 ± 0.007	0.206 ± 0.003
Scaled Semimajor Axis	a/R_s	26.95 ± 0.79	$25.55^{+0.63}_{-0.59}$
Orbital Inclination	i (degrees)	$89.03^{+0.28}_{-0.20}$	88.41 ± 0.16
Impact Parameter	b	$0.45^{+0.08}_{-0.13}$	0.52 ± 0.04
Transit Duration	T_{14} (days)	$0.1216^{+0.0033}_{-0.0030}$	$0.0929^{+0.0017}_{-0.0015}$
Planetary Parameters:			
Mass	M_p ($M_\oplus$; $M_{\rm J}$)	2493 ± 99; 7.84 ± 0.31	3179 ± 100; 10.00 ± 0.32
Mass Ratio	q (%)	1.16 ± 0.06	1.79 ± 0.09
Radius	R_p ($R_\oplus$; $R_{\rm J}$)	$11.59^{+0.61}_{-0.64}$; $1.034^{+0.054}_{-0.057}$	$10.89^{+0.37}_{-0.35}$; $0.972^{+0.033}_{-0.031}$
Density	ρ_p (g cm^{-3})	$8.82^{+1.77}_{-1.32}$	$13.57^{+1.43}_{-1.33}$
Semimajor Axis	a (au)	0.07610 ± 0.00100	$0.05763^{+0.00073}_{-0.00077}$
Planetary Insolation	S ($S_\oplus$)	14.28 ± 1.51	9.97 ± 1.11
Equilibrium Temperature (albedo = 0)	$T_{\rm eq}$ (K)	541 ± 14	495 ± 14
Equilibrium Temperature (albedo = 0.5)	$T_{\rm eq}$ (K)	455 ± 12	416 ± 11

alongside other known transiting giant exoplanets and brown dwarfs around M dwarfs. We queried NASA's Exoplanet Archive (R. L. Akeson et al. 2013) on 2024 August 22 for transiting giant planets around stars with a $T_{\rm eff} < 4100$ K. We also added new discoveries K2-419Ab and TOI-6034b (S. Kanodia et al. 2024), TOI-6383Ab (L. M. Bernabò et al. 2024), and TOI-5688Ab (V. Reji et al. 2025) from the Searching for GEMS survey (S. Kanodia et al. 2024), as well as the newly discovered planets of TOI-762Ab and TIC-46432937b (J. D. Hartman et al. 2024). TOI-2379b is the closest planetary-mass companion comparable to TOI-6303b and TOI-6330b at 5.76 $M_{\rm J}$ (E. M. Bryant et al. 2024), while TOI-1278b is asserted to be a brown dwarf of similar mass of 18.5 $M_{\rm J}$ (E. Artigau et al. 2021).

In Figure 7, we also include recent astrometric + RV discoveries of Gaia-4b and Gaia-5b G. Stefansson et al. (2025), alongside RV discoveries such as GJ 676 Ab (T. Forveille et al. 2011) and GJ 676 Ac (J. Sahlmann et al. 2016). This allows us to paint a fuller picture of known giant planets around M dwarfs. The limitation of the solely RV-measured objects discovered is that they only have a lower mass limit (M_p sin i) compared to the transit discoveries that have bonafide mass measurements (M_p). We compare our discoveries with super-Jupiters around M dwarfs from different detection techniques in Table 5.

The heavy-element content of these objects has shown to be useful in offering insights into the formation of these transiting GEMS (see references in S. Kanodia et al. 2023; M. Delamer et al. 2024). Using the empirical mass–metallicity relations from D. P. Thorngren et al. (2016), we find heavy-element masses of $\sim$200 $M_\oplus$ and $\sim$235 $M_\oplus$ for TOI-6303b and TOI-6330b, respectively. Note that their sample contains notable scatter and uncertainties (both systematic and statistical), such as the equations of state of H/He, sources of heating, and vertical mixing. Such a high metal-content for super-Jupiters is speculated to be a by-product of planet–planet collisions (S. Ginzburg & E. Chiang 2020), though pinning down the exact formation and evolutionary mechanisms for TOI-6303b and TOI-6330b remains a challenge.

In the subsequent sections, we speculate on potential formation scenarios for these massive planets.

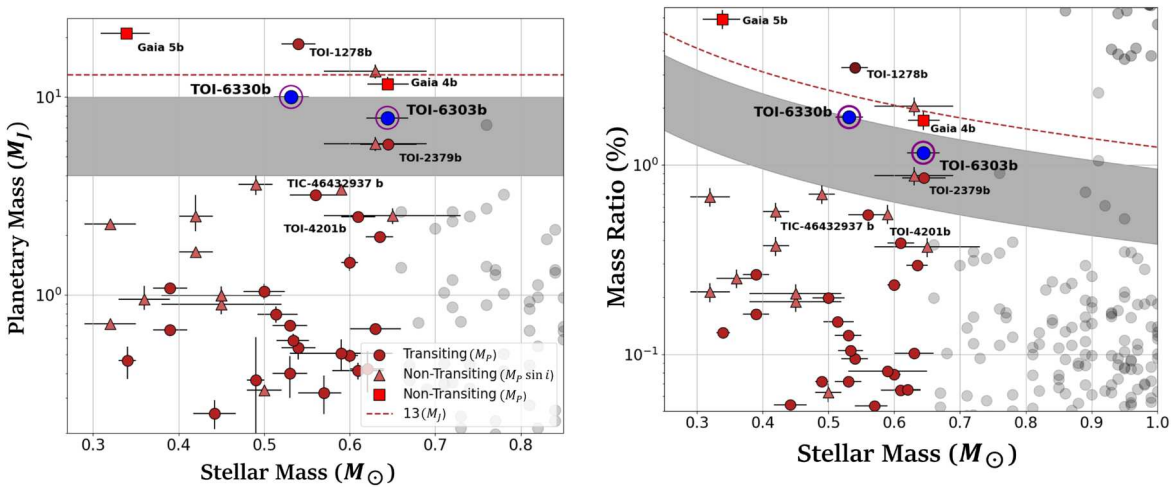

Figure 7. Left: TOI-6303b and TOI-6330b (seen in blue with a ring) on a planetary mass vs. stellar mass plot. The red circles designate transiting GEMS, the red triangles indicate RV-only GEMS, the gray circles indicate FGK planetary companions (NASA Exoplanet Archive; R. L. Akeson et al. 2013), and the red squares are true mass-measured RV objects where astrometry is used to break the sin$i$ degeneracy (G. Stefansson et al. 2025). The gray region between 4 and 10 M_J indicates a sparse region of planetary discoveries made where there is a transition between two major planetary formation paths, core accretion and GI (K. C. Schlaufman 2018). The dotted line indicates the 13 M_J limit where deuterium burning occurs initiates (A. L. D. Etangs & J. J. Lissauer 2022). Right: The mass ratio vs. stellar mass plot for TOI-6303b and TOI-6330b (seen in blue with a purple ring).

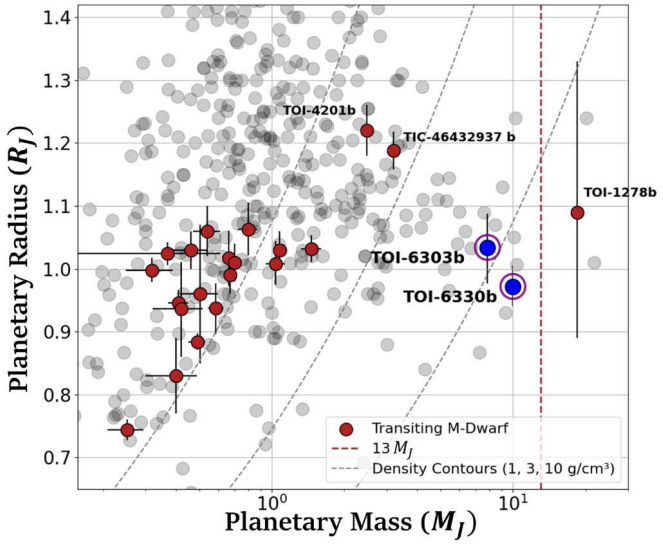

Figure 8. We show TOI-6303b and TOI-6330b (seen in blue with a purple ring) on in the planet mass–radius plane. The red circles designate transiting GEMS and the gray circles indicate FGK planetary companions. We removed NGTS-1b from this plot due to its large uncertainties on the planetary radius from its grazing transit.

4.1. Formation Around M Dwarfs: Core Accretion

Core accretion is the favored formation path for close-in transiting giant exoplanets due to the observed host-star metallicity correlation (D. A. Fischer & J. Valenti 2005; M. Narang et al. 2018; A. Osborn & D. Bayliss 2020). It requires an initial formation of a solid core with a mass of $\sim$10 $M_\oplus$ to initiate a runaway gaseous accretion (H. Mizuno 1980; J. B. Pollack et al. 1996). Around M-dwarf stars, the formation of gas giants through the core-accretion paradigm contains two primary issues: a prolonged formation timescale that would take too long to initiate exponential runaway gaseous accretion with respect to the gas (primarily H/He) lifetime in the disk (G. Laughlin et al. 2004) and a low total dust mass in the protoplanetary disk (due to the disk-to-star mass scaling; S. M. Andrews et al. 2013; I. Pascucci et al. 2016).

Super-Jupiters ($2\,M_J \leqslant M_p \leqslant 10\,M_J$) necessitate formation in the outer regions of the protoplanetary disk (>5 au; C. Mordasini et al. 2009). Since these objects formed around M dwarfs, their orbital timescales are likely much longer, making planetesimal accretion much slower ($\sim$1 Myr), but pebble accretion remains sufficient (M. Lambrechts & A. Johansen 2012; S. Savvidou & B. Bitsch 2023). It is possible that young disks may coagulate more mass in their midplane through self-gravitating spiral waves, allowing for the faster formation of a core massive enough to initiate runaway accretion (N. Haghighipour & A. P. Boss 2003; H. Baehr 2023). Finally, studies have shown that low-mass disks around M dwarfs have a longer lifetime than those around more massive stars (S. Pfalzner et al. 2022). The typical lifetime for protoplanetary disks around M dwarfs is $\sim$2–3 Myr with an upper limit of $\sim$10–20 Myr (A. Ribas et al. 2014). The longer living disks would provide additional time for solid cores and gaseous envelopes to form massive enough to initiate runaway accretion under the core-accretion paradigm.

The primary issue with the core-accretion paradigm when addressing the formation of these objects are the mass limitations. Class II protoplanetary disk masses from the Atacama Large Millimeter/submillimeter Array have a large scatter in the protoplanetary disk masses (M. Ansdell et al. 2016; I. Pascucci et al. 2016; C. F. Manara et al. 2023), and also suffer from systematic underestimation of disk masses (A. Miotello et al. 2022) due to complexities. Primarily, millimeter flux observations of protoplanetary disks may not accurately represent the disk mass due to the optical thickness (A. M. Rilinger et al. 2023) and increased opacity (Y. Liu et al. 2022) of the protoplanetary disks. Furthermore, the Class II disk masses are likely not the primordial mass reservoirs for giant planets (J. S. Greaves & W. K. M. Rice 2010; G. D. Mulders et al. 2021), especially super-Jupiters such as

Table 5
Massive Objects Around M-dwarf Stars in the Transition Between 4 $M_J < M_p < 25\ M_J$

Object Name	M_p (M_J)	M_* ($M_\odot$)	M_p/M_* (%)	Period (days)	M_p or M_p sin$i$	References
TOI-2379b	5.76 ± 0.20	0.645 ± 0.033	0.85	5.469 ± 0.0000023	M_p	E. M. Bryant et al. (2024)
GJ 676 Ab	$5.792^{+0.469}_{-0.477}$	0.626 ± 0.063	0.88	$1051.44^{+0.377}_{-0.400}$	M_p sin$i$	T. Forveille et al. (2011)
TOI-6303b	7.84 ± 0.310	0.644 ± 0.024	1.16	9.485 ± 0.0000162	M_p	This work
Gaia-4b	$11.63^{+0.97}_{-0.82}$	$0.644^{+0.025}_{-0.023}$	1.72	$571.4^{+1.5}_{-1.4}$	M_p	G. Stefansson et al. (2025)
TOI-6330b	10.00 ± 0.315	0.531 ± 0.021	1.79	6.85 ± 0.0000033	M_p	This work
GJ 676 Ac	$13.492^{+1.046}_{-1.127}$	0.626 ± 0.063	2.04	$13921.42^{+1232.34}_{-1514.65}$	M_p sin$i$	J. Sahlmann et al. (2016)
TOI-1278b	18.5 ± 0.5	0.54 ± 0.02	3.27	14.48 ± 0.00021	M_p	E. Artigau et al. (2021)
Gaia-5b	$20.93^{+0.54}_{-0.52}$	$0.339^{+0.027}_{-0.03}$	5.89	358.57 ± 0.2	M_p	G. Stefansson et al. (2025)

Note. We omitted discoveries via direct imaging and required all objects to have parameter values with a precision greater than 3σ.

TOI-6303b and TOI-6330b, with giant planet formation likely beginning much earlier.

Given the low occurrence of GEMS (E. M. Bryant et al. 2023; T. Gan et al. 2023) and high mass ratios, they are clearly outliers of planet formation. Therefore, to explore the feasibility of these super-Jupiters forming through core accretion, instead of considering the median disk dust masses, we estimate the maximum masses that disks can attain before becoming gravitationally unstable based on simulations from Figure 7 in A. P. Boss & S. Kanodia (2023) as ∼10% of the host-star mass. A disk mass of 10% the host-star mass would have a total mass of ∼67 M_J and 56 M_J for TOI-6303 and TOI-6330, respectively. These disks are about 8.5× and 5.5× their respective planet masses, suggesting an overall (mainly gaseous accretion) formation efficiency of 12%–18 %, which is an extremely unlikely efficiency rate compared to that of pebble accretion, which has a formation efficiency of ∼10% (J. W. Lin et al. 2018). While a detailed hydrodynamic simulation is beyond the scope of this paper, studies have shown that the presence of such massive super-Jupiters should open up gaps in protoplanetary disks, which would reduce the gas accretion efficiency and gas mass available for accretion onto these planets (D. N. C. Lin & J. C. B. Papaloizou 1993; G. Bryden et al. 1999; S. Ginzburg & E. Chiang 2020).

We can also estimate the more conventional disk dust mass budget for the massive disks assumed above, with a 1% dust-to-gas mass ratio, to be 200 and 175 $M_\oplus$ for TOI-6303b and TOI-6330b, respectively. In other words, the most massive disks that can stave off gravitational collapse are 10% the host-star mass, and even in this scenario the disk dust masses are only about 100% and 75% the estimated heavy-element content of these planets. Conversely, estimates for the efficiency of pebble accretion efficiency are ∼10% (J. W. Lin et al. 2018), as opposed to the 100% and 133%, respectively, required here.

Even assuming much more favorable formation efficiency estimates would necessitate very massive disks that are ≫10% the stellar mass, or uncharacteristically metal-rich. This might indeed be the case for TOI-6303, which is likely metal-rich, as opposed to TOI-6330, which is closer to Solar metallicity.

In summary, such massive planets (1.16%–1.79% mass ratios) are difficult to explain under the core-accretion paradigm without very massive disks (>10%) that should be susceptible to gravitational collapse. This simple argument is agnostic of the limitations of protoplanetary disk mass measurements, as well as the assumptions for the epoch at which planet formation should begin.

4.2. Formation Around M Dwarfs: GI

With these limitations, the GI paradigm provides an alternative mechanism, taking place earlier, in class 0/I disks or the protostellar phase (G. P. Kuiper 1951; A. G. W. Cameron 1978; A. P. Boss 1997).

Compared to previous GEMS discoveries, TOI-6303b and TOI-6330b are both a much larger percentage of their host-star's mass (see Figure 7). There is a sparse region of planetary discoveries these objects fall into, where, for FGK stars, we see a shift in formation paths from core accretion to GI for objects between ∼4 and 10 M_J. Studies have shown this region exists around solar-type stars with metallicities ranging from ∼±0.5 [Fe/H], which includes a noticeable trend: as the metallicities increase, there is an increase in giant planet detections (D. A. Fischer & J. Valenti 2005; K. C. Schlaufman 2018; J. Maldonado et al. 2019).

GI can occur in a more massive Class 0/I protostellar disk, enabling it to satisfy the mass budget limitations, along with formation timescales on the order of $\sim 10^3$ yr (A. P. Boss 1997). The instability model begins within the protostellar or class 0/I disks and similarly requires ≳10% of the disk mass to initiate gravitational collapse and clump formation (A. P. Boss 2006, 2011). Fragmentation of the disk leads to self-gravitating large clumps and serves as the beginning stage of a forming giant planet (For a full review of GI see R. H. Durisen et al. 2007; K. Kratter & G. Lodato 2016). The formation of a planet through GI requires cooler temperatures to allow for efficient gravitational collapse through a lack of thermal pressure, causing the collapse to occur at large distances from the host star.

4.3. Migration

The close-in nature of these planetary-mass companions requires migration inward from their formation distances. The low eccentricity for TOI-6303b (0.02 ± 0.02) is suggestive of a more dynamically quiet migration scenario, potentially through interactions with the disk. (W. Kley & R. P. Nelson 2012; R. I. Dawson & J. A. Johnson 2018). Conversely, TOI-6330b's higher eccentricity (0.34 ± 0.01) is more indicative of high-eccentricity tidal migration (C. Beaugé & D. Nesvorný 2012). R. I. Dawson & J. A. Johnson (2018) define high-eccentricity tidal migration as a two-step process

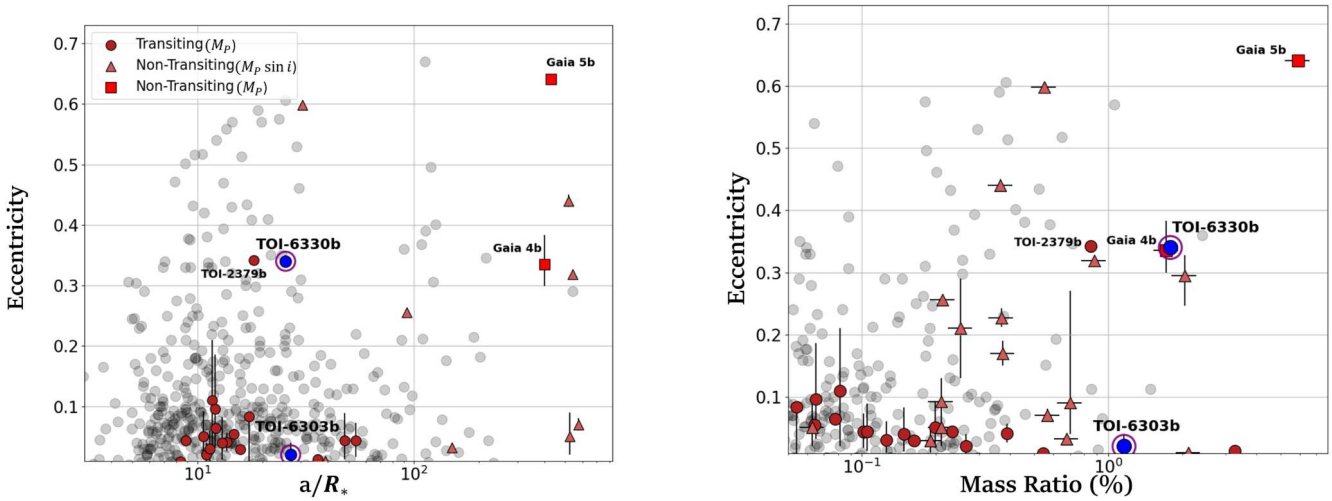

Figure 9. Left: The eccentricity vs. semimajor axis over the stellar radius for TOI-6303b and TOI-6330b (seen in blue with a purple ring). The red circles indicate the transiting M-dwarf planetary companions and the gray circles are the FGK transiting companions as used in Figure 7. Both TOI-6303b and TOI-6330b are at similar values for a/R_* (26.95 ± 0.79 and $25.55\ ^{+0.63}_{-0.59}$, respectively) but have different eccentricity values (0.02 ± 0.02 and 0.34 ± 0.01). Right: Similar to left plot but evaluating eccentricity vs. mass ratio with their M_p/M_* being 1.16% for TOI-6303b and 1.79% for TOI-6330b.

where the planet migrates and is circularized through tidal interactions with the host star. This migration can appear in two facets: planet–planet scattering (e.g., F. A. Rasio & E. B. Ford 1996; S. Chatterjee et al. 2008) and secular interactions.

Planet–planet scattering can occur where planets form in a tightly packed system (M. Jurić & S. Tremaine 2008) or a stellar fly (M. M. Shara et al. 2016), but it is unlikely that a planet obtains its low-period orbit through solely scattering. It requires many encounters for a planet to obtain its eccentricity. Additionally, an undetected planet may help maintain a high eccentricity (F. C. Adams & G. Laughlin 2006). Secular interactions are the exchange of angular momentum through planets that are widely separated from one another (R. I. Dawson & J. A. Johnson 2018). This migration takes thousands to millions of years to occur with two primary methods in swapping angular momentum: periodically (e.g., C. Petrovich 2015a) and chaotically (e.g., A. S. Hamers et al. 2017), with chaotically requiring three or more planets. For further discussion on both migration techniques see R. I. Dawson & J. A. Johnson (2018). It is important to note that we do not detect any signs of an additional companion to TOI-6330.

Most transiting GEMS have low eccentricity values, ostensibly due to their short orbital periods, lower host-star masses, and lower planetary masses that lead to shorter circularization timescales (Figure 9). TOI-6303 b has a low eccentricity that is comparable to the majority of GEMS, but TOI-6330b is among the outliers. We estimate the circularization timescales for TOI-6303b and TOI-6330b using Equations (3) and (4) from C. M. Persson et al. (2019), which derives the circularization timescale, τ_e using Equations (1) and (2) from B. Jackson et al. (2008).

$$\frac{1}{\tau_e} = \frac{1}{\tau_{e,*}} + \frac{1}{\tau_{e,P}}, \tag{1}$$

$$\frac{1}{\tau_{e,*}} = a_P^{-13/2} \frac{171}{16} \sqrt{\frac{G}{M_*}} \frac{R_*^5 M_P}{Q_*}, \tag{2}$$

$$\frac{1}{\tau_{e,P}} = a_P^{-13/2} \frac{63}{4} \sqrt{G M_*^3} \frac{R_P^5}{Q_P M_P}. \tag{3}$$

We assume $Q_P \sim 10^5$ and $Q_* \sim 10^7$(See P. Goldreich & S. Soter 1966; V. Lainey 2016). This yields a $\tau_e \sim$ 27 Gyr and 10 Gyr for TOI-6303b and TOI-6330b, respectively, which is much longer than the estimated age for these systems. Lower assumed Q_P would make the circularization process more efficient and reduce these formation timescales. We estimate τ_e of ~3 Gyr and ~1 Gyr, respectively, for an assumed Q_P of 10^4; however, this value would be much lower than the assumed Q_P value for Saturn with a mass of 0.3 M_J of 6×10^4 (P. Goldreich & S. Soter 1966), where Q_P is expected to increase with planetary mass. While we speculate on these timescales, we also note that the actual efficiency of the processes is heavily dependent on the mass distribution in these giant planet interiors, which is poorly constrained for such super-Jupiters. With circularization timescales larger than the age of both systems, we look to previously mentioned formation mechanisms to explain the eccentricities of TOI-6303b and TOI-6330b.

Under the GI formation scenario, it is also possible for the planet TOI-6330b to perturb spiral waves in the primordial marginally unstable disk (S. Paardekooper et al. 2023), the feedback from which could result in moderate eccentricities consistent with those seen here (see Figure 6; A. P. Boss 2024). Conversely, due to the preponderance of GI to enable the formation of >1 compact objects (planets or brown dwarfs) in a system, the eccentricity seen here could also be ascribed to scattering events such as those described above and seen in simulations (A. P. Boss 2023).

5. Conclusion

We present the discovery of TOI-6303b and TOI-6330b, the two most massive transiting giant exoplanets around early M dwarfs. These planetary-mass companions were first identified

by TESS photometry and were characterized by ground-based photometry, RVs, and speckle imaging follow-up.

TOI-6303b and TOI-6330b have mass ratios of 1.16% and 1.79% with their host stars, respectively, requiring a formation efficiency of 12%–18% to have successfully formed through core accretion in protoplanetary disks right on the cusp of GI (67 M_J and 56 M_J, respectively, 10% disk-to-star mass ratio). Furthermore, even in these massive disks, the dust masses are only 100% and 75% the estimated heavy-element content of TOI-6303b and TOI-6330b, respectively. Even attributing the most favorable formation efficiency to these objects would require massive protoplanetary disks that would be on the cusp of gravitational collapse, making GI the more likely formation pathway.

These objects share many similarities but have differing eccentricities that could provide insight into their possible formation and migration history. TOI-6303b has an approximately circular orbit, which is representative of gas-disk migration, while TOI-6330b has a relatively eccentric orbit, which indicates an alternate migration technique such as planet–planet scattering or secular interactions. The detection of TOI-6303b and TOI-6330b helps investigate a sparse region of planetary discoveries and provides insight into giant planet formation around M-dwarf stars.

Acknowledgments

We would like to thank the anonymous referee for their time and effort in providing comments that have significantly improved this paper.

Some of the observations in this paper made use of the NN-EXPLORE Exoplanet and Stellar Speckle Imager (NESSI). NESSI was funded by the NASA Exoplanet Exploration Program and the NASA Ames Research Center. NESSI was built at the Ames Research Center by Steve B. Howell, Nic Scott, Elliott P. Horch, and Emmett Quigley.

The Pennsylvania State University campuses are located on the original homelands of the Erie, Haudenosaunee (Seneca, Cayuga, Onondaga, Oneida, Mohawk, and Tuscarora), Lenape (Delaware Nation, Delaware Tribe, Stockbridge-Munsee), Shawnee (Absentee, Eastern, and Oklahoma), Susquehannock, and Wahzhazhe (Osage) Nations. As a land grant institution, we acknowledge and honor the traditional caretakers of these lands and strive to understand and model their responsible stewardship. We also acknowledge the longer history of these lands and our place in that history.

These results are based on observations obtained with the HPF Spectrograph on the HET. We acknowledge support from NSF grants AST-1006676, AST-1126413, AST-1310885, AST-1310875, ATI-2009889, ATI-2009982, AST-2108512, and AST-2108801, and the NASA Astrobiology Institute (NNA09DA76A) in the pursuit of precision radial velocities in the NIR. The HPF team also acknowledges support from the Heising–Simons Foundation via grant 2017-0494. The Hobby–Eberly Telescope is a joint project of the University of Texas at Austin, the Pennsylvania State University, Ludwig-Maximilians-Universität München, and Georg-August Universität Gottingen. The HET is named in honor of its principal benefactors, William P. Hobby and Robert E. Eberly. The HET collaboration acknowledges the support and resources from the Texas Advanced Computing Center. We thank the resident astronomers and telescope operators at the HET for the skillful execution of our observations with HPF. We would like to acknowledge that the HET is built on Indigenous land. Moreover, we would like to acknowledge and pay our respects to the Carrizo and Comecrudo, Coahuiltecan, Caddo, Tonkawa, Comanche, Lipan Apache, Alabama–Coushatta, Kickapoo, Tigua Pueblo, and all the American Indian and Indigenous Peoples and communities who have been or have become a part of these lands and territories in Texas, here on Turtle Island.

WIYN is a joint facility of the University of Wisconsin–Madison, Indiana University, NSF's NOIRLab, the Pennsylvania State University, Purdue University, University of California-Irvine, and the University of Missouri.

The authors are honored to be permitted to conduct astronomical research on Iolkam Du'ag (Kitt Peak), a mountain with particular significance to the Tohono O'odham. Data presented herein were obtained at the WIYN Observatory from telescope time allocated to NN-EXPLORE (PI-Kanodia; 2023B-438370, 2024A-103024) through the scientific partnership of NASA, the NSF, and NOIRLab.

This work has made use of data from the European Space Agency (ESA) mission Gaia (https://www.cosmos.esa.int/gaia), processed by the Gaia Data Processing and Analysis Consortium (DPAC, https://www.cosmos.esa.int/web/gaia/dpac/consortium). Funding for the DPAC has been provided by national institutions, in particular the institutions participating in the Gaia Multilateral Agreement.

Some of the observations in this paper were obtained with the Samuel Oschin Telescope 48 inch and the 60 inch Telescope at the Palomar Observatory as part of the ZTF project. ZTF is supported by the NSF under grant No. AST-2034437 and a collaboration including Caltech, IPAC, the Weizmann Institute for Science, the Oskar Klein Center at Stockholm University, the University of Maryland, Deutsches Elektronen-Synchrotron and Humboldt University, the TANGO Consortium of Taiwan, the University of Wisconsin at Milwaukee, Trinity College Dublin, Lawrence Livermore National Laboratories, and IN2P3, France. Operations are conducted by COO, IPAC, and UW.

Computations for this research were performed on the Pennsylvania State University's Institute for Computational and Data Sciences Advanced CyberInfrastructure (ICDS-ACI). This content is solely the responsibility of the authors and does not necessarily represent the views of the Institute for Computational and Data Sciences.

The Center for Exoplanets and Habitable Worlds is supported by the Pennsylvania State University, the Eberly College of Science, and the Pennsylvania Space Grant Consortium.

Some of the data presented in this paper were obtained from MAST at STScI. Support for MAST for non-HST data is provided by the NASA Office of Space Science via grant NNX09AF08G and by other grants and contracts.

This work includes data collected by the TESS mission, which are publicly available from MAST (MAST Team 2021a, 2021b). Funding for the TESS mission is provided by the NASA Science Mission directorate. This research made use of the (i) NASA Exoplanet Archive, which is operated by Caltech, under contract with NASA under the Exoplanet Exploration Program, (ii) SIMBAD database, operated at CDS, Strasbourg, France, (iii) NASA's Astrophysics Data System Bibliographic Services, and (iv) data from 2MASS, a joint project of the University of Massachusetts and IPAC at Caltech, funded by NASA and the NSF.

This research has made use of the SIMBAD database, operated at CDS, Strasbourg, France, and NASA's Astrophysics Data System Bibliographic Services.

This research has made use of the Exoplanet Follow-up Observation Program (ExoFOP; DOI: 10.26134/ExoFOP5; NExScI 2022) website, which is operated by the California Institute of Technology, under contract with the National Aeronautics and Space Administration under the Exoplanet Exploration Program.

C.I.C. acknowledges support by an appointment to the NASA Postdoctoral Program at the Goddard Space Flight Center, administered by USRA through a contract with NASA.

Facilities: Gaia, HET (HPF), WIYN 3.5m (NESSI), Shane (ShARCS), RBO, Keeble, APO/ARCTIC, ZTF, TESS, Exoplanet Archive.

Software: `ArviZ` (R. Kumar et al. 2019), AstroImageJ (K. A. Collins et al. 2017), `astropy` (T. P. Robitaille et al. 2013; Astropy Collaboration et al. 2018), `barycorrpy` (S. Kanodia & J. Wright 2018), `celerite2` (D. Foreman-Mackey et al. 2017; D. Foreman-Mackey 2018), `eleanor`(A. D. Feinstein et al. 2019), `EXOFASTv2` (J. D. Eastman et al. 2019), `exoplanet` (D. Foreman-Mackey et al. 2021a, 2021b), `HPF-SpecMatch` (G. Stefansson et al. 2020), `HxRGproc` (J. P. Ninan et al. 2018), `ipython` (F. Pérez & B. E. Granger 2007), `lightkurve` (Lightkurve Collaboration et al. 2018), `matplotlib` (J. D. Hunter 2007), `numpy` (C. R. Harris et al. 2020), `pandas` (W. McKinney 2010), `photutils` (L. Bradley et al. 2020), `pyastrotools` (S. Kanodia 2023), `PyMC3` (J. Salvatier et al. 2016), `scipy` (P. Virtanen et al. 2020), `SERVAL`(M. Zechmeister et al. 2018), `Theano` (The Theano Development Team et al. 2016).

ORCID iDs

Andrew Hotnisky https://orcid.org/0009-0000-1825-4306
Shubham Kanodia https://orcid.org/0000-0001-8401-4300
Jessica Libby-Roberts https://orcid.org/0000-0002-2990-7613
Suvrath Mahadevan https://orcid.org/0000-0001-9596-7983
Caleb I. Cañas https://orcid.org/0000-0003-4835-0619
Arvind F. Gupta https://orcid.org/0000-0002-5463-9980
Te Han https://orcid.org/0000-0002-7127-7643
Henry A. Kobulnicky https://orcid.org/0000-0002-4475-4176
Alexander Larsen https://orcid.org/0000-0002-2401-8411
Paul Robertson https://orcid.org/0000-0003-0149-9678
Michael Rodruck https://orcid.org/0009-0009-4977-1010
Gudmundur Stefansson https://orcid.org/0000-0001-7409-5688
William D. Cochran https://orcid.org/0000-0001-9662-3496
Megan Delamer https://orcid.org/0000-0003-1439-2781
Scott A. Diddams https://orcid.org/0000-0002-2144-0764
Rachel B. Fernandes https://orcid.org/0000-0002-3853-7327
Samuel Halverson https://orcid.org/0000-0003-1312-9391
Leslie Hebb https://orcid.org/0000-0003-1263-8637
Andrea S.J. Lin https://orcid.org/0000-0002-9082-6337
Andrew Monson https://orcid.org/0000-0002-0048-2586
Joe P. Ninan https://orcid.org/0000-0001-8720-5612
Arpita Roy https://orcid.org/0000-0001-8127-5775
Christian Schwab https://orcid.org/0000-0002-4046-987X

References

Adams, F. C., & Laughlin, G. 2006, ApJ, 649, 1004
Akeson, R. L., Chen, X., Ciardi, D., et al. 2013, PASP, 125, 989
Andrews, S. M., Rosenfeld, K. A., Kraus, A. L., & Wilner, D. J. 2013, ApJ, 771, 129
Ansdell, M., Williams, J. P., van der Marel, N., et al. 2016, ApJ, 828, 46
Artigau, E., Hebrard, G., Cadieux, C., et al. 2021, AJ, 162, 144
Astropy Collaboration, Price-Whelan, A. M., Sipőcz, B. M., et al. 2018, AJ, 156, 123
Baehr, H. 2023, MNRAS, 523, 3348
Bailer-Jones, C. A. L., Rybizki, J., Fouesneau, M., Demleitner, M., & Andrae, R. 2021, AJ, 161, 147
Beaugé, C., & Nesvorný, D. 2012, ApJ, 751, 119
Belokurov, V., Penoyre, Z., Oh, S., et al. 2020, MNRAS, 496, 1922
Bergsten, G. J., Pascucci, I., Hardegree-Ullman, K. K., et al. 2023, AJ, 166, 234
Bernabò, L. M., Kanodia, S., Cañas, C. I., et al. 2024, AJ, 168, 273
Bitsch, B., & Izidoro, A. 2023, A&A, 674, A178
Boss, A. P. 1997, Sci, 276, 1836
Boss, A. P. 2006, ApJ, 643, 501
Boss, A. P. 2011, ApJ, 731, 74
Boss, A. P. 2023, ApJ, 943, 101
Boss, A. P. 2024, ApJ, 969, 157
Boss, A. P., & Kanodia, S. 2023, ApJ, 956, 4
Bradley, L., Sipőcz, B., Robitaille, T., et al. 2020, astropy/photutils: v1.0.0, Zenodo, doi:10.5281/zenodo.4044744
Bryant, E. M., Bayliss, D., Hartman, J. D., et al. 2024, MNRAS, 533, 3893
Bryant, E. M., Bayliss, D., & Van Eylen, V. 2023, MNRA, 521, 3663
Bryden, G., Chen, X., Lin, D. N. C., Nelson, R. P., & Papaloizou, J. C. B. 1999, ApJ, 514, 344
Cameron, A. G. W. 1978, M&P, 18, 5
Cañas, C. I., Stefansson, G., Kanodia, S., et al. 2020, AJ, 160, 147
Cañas, C. I., Mahadevan, S., Bender, C. F., et al. 2022, AJ, 163, 89
Chabrier, G., Johansen, A., Janson, M., & Rafikov, R. 2014, in Protostars and Planets VI, ed. H. Beuther et al. (Tucson, AZ: Univ. Arizona Press), 619
Chambers, K. C., Magnier, E. A., Metcalfe, N., et al. 2016, arXiv:1612.05560
Chatterjee, S., Ford, E. B., Matsumura, S., & Rasio, F. A. 2008, ApJ, 686, 580
Childs, A. C., Martin, R. G., & Livio, M. 2022, ApJL, 937, L41
Childs, A. C., Quintana, E., Barclay, T., & Steffen, J. H. 2019, MNRAS, 485, 541
Collins, K. A., Kielkopf, J. F., Stassun, K. G., & Hessman, F. V. 2017, AJ, 153, 77
Cutri, R. M., Skrutskie, M. F., van Dyk, S., et al. 2003, The IRSA 2MASS All-Sky Point Source Catalog, NASA/IPAC, http://irsa.ipac.caltech.edu/applications/Gator/
Dawson, R. I., & Johnson, J. A. 2018, ARA&A, 56, 175
Delamer, M., Kanodia, S., Cañas, C. I., et al. 2024, ApJ, 962, L22
Dressing, C. D., & Charbonneau, D. 2015, ApJ, 807, 45
Durisen, R. H., Boss, A. P., Mayer, L., et al. 2007, in Protostars and Planets V, ed. B. Reipurth, D. Jewitt, & K. Keil (Tucson, AZ: Univ. Arizona Press), 607
Eastman, J. D., Rodriguez, J. E., Agol, E., et al. 2019, arXiv:1907.09480
Etangs, A. L. D., & Lissauer, J. J. 2022, NewAR, 94, 101641
Feinstein, A. D., Montet, B. T., Foreman-Mackey, D., et al. 2019, PASP, 131, 094502
Fischer, D. A., & Valenti, J. 2005, ApJ, 622, 1102
Ford, E. B. 2006, ApJ, 642, 505
Foreman-Mackey, D. 2018, RNAAS, 2, 31
Foreman-Mackey, D., Agol, E., Ambikasaran, S., & Angus, R. 2017, AJ, 154, 220
Foreman-Mackey, D., Luger, R., Agol, E., et al. 2021a, JOSS, 6, 3285
Foreman-Mackey, D., Savel, A., Luger, R., et al. 2021b, Exoplanet-Dev/Exoplanet, v0.4.4, Zenodo, doi:10.5281/zenodo.1998447
Forveille, T., Bonfils, X., Lo Curto, G., et al. 2011, A&A, 526, A141
Gaia Collaboration, Brown, A. G. A., Vallenari, A., et al. 2021, A&A, 649, A1
Gan, T., Wang, S. X., Wang, S., et al. 2023, AJ, 165, 17
Ginzburg, S., & Chiang, E. 2020, MNRAS, 498, 680
Goldreich, P., & Soter, S. 1966, Icar, 5, 375
Greaves, J. S., & Rice, W. K. M. 2010, MNRAS, 407, 1981
Green, G. M., Schlafly, E., Zucker, C., Speagle, J. S., & Finkbeiner, D. 2019, ApJ, 887, 93
Haghighipour, N., & Boss, A. P. 2003, ApJ, 598, 1301
Hamers, A. S., Antonini, F., Lithwick, Y., Perets, H. B., & Portegies Zwart, S. F. 2017, MNRAS, 464, 688
Hardegree-Ullman, K. K., Cushing, M. C., Muirhead, P. S., & Christiansen, J. L. 2019, AJ, 158, 75
Harris, C. R., Millman, K. J., van der Walt, S. J., et al. 2020, Natur, 585, 357
Hartman, J. D., Bayliss, D., Brahm, R., et al. 2024, AJ, 168, 202

Henden, A. A., Levine, S., Terrell, D., et al. 2018, APASS Data Release 10 232.06, American Astronomical Society
Henry, T. J., Jao, W.-C., Subasavage, J. P., et al. 2006, AJ, 132, 2360
Hobson, M. J., Jordán, A., Bryant, E. M., et al. 2023, ApJL, 946, L4
Howell, S. B., Everett, M. E., Sherry, W., Horch, E., & Ciardi, D. R. 2011, AJ, 142, 19
Hsu, D. C., Ford, E. B., & Terrien, R. 2020, MNRAS, 498, 2249
Huang, C. X., Vanderburg, A., Pál, A., et al. 2020, RNAAS, 4, 204
Huehnerhoff, J., Ketzeback, W., Bradley, A., et al. 2016, Proc. SPIE, 9908, 99085H
Hunter, J. D. 2007, CSE, 9, 90
Ida, S., & Lin, D. N. C. 2005, ApJ, 626, 1045
Jackson, B., Greenberg, R., & Barnes, R. 2008, ApJ, 678, 1396
Jurić, M., & Tremaine, S. 2008, ApJ, 686, 603
Kanodia, S. 2023, shbhuk/pyastrotools: v0.3, Zenodo, doi:10.5281/zenodo.7685628
Kanodia, S., Cañas, C. I., Mahadevan, S., et al. 2024, AJ, 167, 161
Kanodia, S., Mahadevan, S., Libby-Roberts, J., et al. 2023, AJ, 165, 120
Kanodia, S., Mahadevan, S., Ramsey, L. W., et al. 2018, Proc. SPIE, 10702, 107026Q
Kanodia, S., & Wright, J. 2018, RNAAS, 2, 4
Kasper, D. H., Ellis, T. G., Yeigh, R. R., et al. 2016, PASP, 128, 105005
Kasting, J. F., Whitmire, D. P., & Reynolds, R. T. 1993, Icar, 101, 108
Kley, W., & Nelson, R. P. 2012, ARA&A, 50, 211
Kopparapu, R. K., Ramirez, R., Kasting, J. F., et al. 2013, ApJ, 765, 131
Kratter, K., & Lodato, G. 2016, ARA&A, 54, 271
Kuiper, G. P. 1951, PNAS, 37, 1
Kumar, R., Carroll, C., Hartikainen, A., & Martin, O. A. 2019, JOSS, 4, 1143
Kunimoto, M., Winn, J. N., Ricker, G. R., & Vanderspek, R. 2022, AJ, 163, 290
Lainey, V. 2016, CeMDA, 126, 145
Lambrechts, M., & Johansen, A. 2012, A&A, 544, A32
Laughlin, G., Bodenheimer, P., & Adams, F. C. 2004, ApJL, 612, L73
Lightkurve Collaboration, Cardoso, J. V. d. M., Hedges, C., et al., 2018 Lightkurve: Kepler and TESS time series analysis in Python, Astrophysics Source Code Library, ascl:1812.013
Lin, D. N. C., & Papaloizou, J. C. B. 1993, in Protostars and Planets III, ed. E. H. Levy & J. I. Lunine (Tucson, AZ: Univ. Arizona Press), 749
Lin, J. W., Lee, E. J., & Chiang, E. 2018, MNRAS, 480, 4338
Liu, Y., Linz, H., Fang, M., et al. 2022, A&A, 668, A175
Magnier, E. A., Chambers, K. C., Flewelling, H. A., et al. 2020, ApJS, 251, 3
Mahadevan, S., Ramsey, L., Bender, C., et al. 2012, Proc. SPIE, 8446, 84461S
Mahadevan, S., Ramsey, L. W., Terrien, R., et al. 2014, Proc. SPIE, 9147, 91471G
Maldonado, J., Villaver, E., Eiroa, C., & Micela, G. 2019, A&A, 624, A94
Manara, C. F., Ansdell, M., Rosotti, G. P., et al. 2023, in ASP Conf. Ser. 534, Protostars and Planets VII, ed. S. Inutsuka (San Francisco, CA: ASP), 539
Mann, A. W., Dupuy, T., Kraus, A. L., et al. 2019, ApJ, 871, 63
Mann, A. W., Feiden, G. A., Gaidos, E., Boyajian, T., & von Braun, K. 2015, ApJ, 804, 64
Masci, F. J., Laher, R. R., Rusholme, B., et al. 2019, PASP, 131, 018003
MAST Team 2021a, TESS "Fast" Light Curves—All Sectors, STScI/MAST, doi:10.17909/t9-st5g-3177
MAST Team 2021b, TESS Light Curves: All Sectors, STScI/MAST, doi:10.17909/t9-nmc8-f686
McKinney, W. 2010, in Proc. 9th Python in Science Conf., ed. S. van der Walt & J. Millman (Austin, TX: SciPy Proceedings), 61, 10.25080/Majora-92bf1922-00a
Ment, K., & Charbonneau, D. 2023, AJ, 165, 265
Metcalf, A. J., Anderson, T., Bender, C. F., et al. 2019, Optic, 6, 233
Miotello, A., Kamp, I., Birnstiel, T., Cleeves, L. I., & Kataoka, A. 2022, in ASP Conf. Ser. 534, Protostars and Planets VII, ed. S. Inutsuka (San Francisco, CA: ASP), 501
Mizuno, H. 1980, PThPh, 64, 544
Monson, A. J., Beaton, R. L., Scowcroft, V., et al. 2017, AJ, 153, 96
Mordasini, C., Alibert, Y., & Benz, W. 2009, A&A, 501, 1139
Mulders, G. D., Pascucci, I., Ciesla, F. J., & Fernandes, R. B. 2021, ApJ, 920, 66
Narang, M., Manoj, P., Furlan, E., et al. 2018, AJ, 156, 221
NExScI 2022, Exoplanet Follow-up Observing Program Web Service, IPAC, doi:10.26134/EXOFOP5
Ninan, J. P., Bender, C. F., Mahadevan, S., et al. 2018, Proc. SPIE, 0709, 107092U
Osborn, A., & Bayliss, D. 2020, MNRAS, 491, 4481
Paardekooper, S., Dong, R., Duffell, P., et al. 2023, in ASP Conf. Ser. 534, Protostars and Planets VII, ed. S. Inutsuka (San Francisco, CA: ASP), 685
Pascucci, I., Testi, L., Herczeg, G. J., et al. 2016, ApJ, 831, 125
Passegger, V. M., Bello-Garcìa, A., Ordieres-Meré, J., et al. 2022, A&A, 658, A194
Pérez, F., & Granger, B. E. 2007, CSE, 9, 21
Persson, C. M., Csizmadia, S., Mustill, A. J., et al. 2019, A&A, 628, A64
Petrovich, C. 2015a, ApJ, 805, 75
Pfalzner, S., Dehghani, S., & Michel, A. 2022, ApJL, 939, L10
Pollack, J. B., Hubickyj, O., Bodenheimer, P., et al. 1996, Icar, 124, 62
Ramsey, L. W., Adams, M. T., Barnes, T. G., et al. 1998, Proc. SPIE, 3352, 34
Rasio, F. A., & Ford, E. B. 1996, Sci, 274, 954
Reji, V., Kanodia, S., Ninan, J., et al. 2025, AJ, 169, 187
Reylé, C., Jardine, K., Fouqué, P., et al. 2021, A&A, 650, A201
Ribas, A., Merin, B., Bouy, H., & Maud, L. T. 2014, A&A, 561, A54
Ricker, G. R., Winn, J. N., Vanderspek, R., et al. 2014, JATIS, 1, 014003
Rilinger, A. M., Espaillat, C. C., Xin, Z., et al. 2023, ApJ, 944, 66
Robitaille, T. P., Tollerud, E. J., Greenfield, P., et al. 2013, A&A, 558, A33
Sahlmann, J., Lazorenko, P. F., Ségransan, D., et al. 2016, A&A, 595, A77
Salvatier, J., Wiecki, T. V., & Fonnesbeck, C. 2016, PeerJ, 2, e55
Santos, N. C., Adibekyan, V., Figueira, P., et al. 2017, A&A, 603, A30
Savvidou, S., & Bitsch, B. 2023, A&A, 679, A42
Scalo, J., Kaltenegger, L., Segura, A., et al. 2007, AsBio, 7, 85
Schlaufman, K. C. 2018, ApJ, 853, 37
Schlecker, M., Pham, D., Burn, R., et al. 2021, A&A, 656, A73
Scott, N. J., Howell, S. B., Horch, E. P., & Everett, M. E. 2018, PASP, 130, 054502
Shara, M. M., Hurley, J. R., & Mardling, R. A. 2016, ApJ, 816, 59
Shetrone, M., Cornell, M. E., Fowler, J. R., et al. 2007, PASP, 119, 556
Srinath, S., McGurk, R., Rockosi, C., et al. 2014, Proc. SPIE, 9148, 91482Z
Stassun, K. G., Oelkers, R. J., Pepper, J., et al. 2018, AJ, 156, 102
Stefansson, G., Cañas, C., Wisniewski, J., et al. 2020, AJ, 159, 100
Stefansson, G., Hearty, F., Robertson, P., et al. 2016, ApJ, 833, 175
Stefansson, G., Mahadevan, S., Hebb, L., et al. 2017, ApJ, 848, 9
Stefánsson, G., Mahadevan, S., Miguel, Y., et al. 2023, Sci, 382, 1031
Stefansson, G., Mahadevan, S., Winn, J., et al. 2025, AJ, 169, 107
The Theano Development Team, Al-Rfou, R., Alain, G., et al. 2016, arXiv:1605.02688
Thorngren, D. P., Fortney, J. J., Murray-Clay, R. A., & Lopez, E. D. 2016, ApJ, 831, 64
Virtanen, P., Gommers, R., Oliphant, T. E., et al. 2020, NatMe, 17, 261
Wright, E. L., Eisenhardt, P. R. M., Mainzer, A. K., et al. 2010, AJ, 140, 1868
Wright, J. T., & Eastman, J. D. 2014, PASP, 126, 838
Zechmeister, M., Reiners, A., Amado, P. J., et al. 2018, A&A, 609, A12
Ziegler, C., Tokovinin, A., Briceño, C., et al. 2020, AJ, 159, 19